Supplementary Materials

Electronic structure modulation through superexchange in spinel oxides for simultaneous NO_x and propane removal

Jiahui Wu[1,2], Yaqin Hou[1,2,*], Shuang Ma[1,2], Yujing Han[1,2], Ke Liu[1,2], Yan Cui[1,2], Weiren Bao[3], Jiancheng Wang[4], Zhanggen Huang[1,2,*]

[1]State Key Laboratory of Coal Conversion, Institute of Coal Chemistry, Chinese Academy of Sciences, Taiyuan 030001, Shanxi, China.

[2]University of Chinese Academy of Sciences, Beijing 100049, China.

[3]State Key Laboratory of Clean and Efficient Utilization, College of Chemistry and Chemical Engineering, Taiyuan University of Technology, Taiyuan 030024, Shanxi, China.

[4]Shanxi Key Laboratory of Complex Air Pollution Control and Carbon Reduction, College of Environmental Science and Engineering, Taiyuan University of Technology, Taiyuan 030024, Shanxi, China.

[*]**Correspondence to:** Dr. Yaqin Hou, Prof. Zhanggen Huang, State Key Laboratory of Coal Conversion, Institute of Coal Chemistry, Chinese Academy of Sciences, Taiyuan 030001, Shanxi, China. E-mail: houyaqin@sxicc.ac.cn; zghuang@sxicc.ac.cn.

2.2. Catalyst characterizations

The JSM-7001F field emission scanning electron microscope (SEM) was used to analyze the surface morphology of the samples. High resolution transmission electron microscopy (HRTEM) images were obtained from JEM-2100F field emission transmission electron microscope under 200 kV acceleration voltage. X-ray diffraction patterns (XRD) captured on a Bruker D8 Advance X-ray diffractometer using Cu Ka radiation (40 mA, 40 kV). All the catalysts were scanned at 2θ range between 5° to 90°. Nitrogen adsorption-desorption isotherms were recorded at 77 K using a Quantachrome Auto Sorb iQ-MP. Before the measurement, the samples were degassed and pretreated at 300 °C for 12 h. The surface areas, pore volumes, and average pore diameters were calculated by the multipoint Brunauer-Emmett-Teller (BET) analysis of the adsorption isotherm. X-ray photoelectron spectra (XPS) were recorded on a Thermo Scientific K-Alpha photoelectron spectroscopy with Al Kα X-ray radiation (1486.6 eV). The charging effect was corrected by adjusting the binding energy of C 1 s to 284.6 eV. The Raman spectra were collected on a WITec alpha300 RAS microlaser Raman spectrometer using an argon ion laser source with λ at 532 nm. NH_3 temperature-programmed desorption (NH_3-TPD) was per-formed on the fixed-bed reactor. The catalyst (300 mg) was pretreated in a N_2 (200 mL·min^{-1}) at 300 °C for 1 h, and then cooled to 50 °C. Sample was treated with mixture of N_2 and 500 ppm NH_3 (200 mL·min^{-1}) for 1 h to achieve adsorption saturation. The gas was switched back to N_2 (200 mL·min^{-1}) for 0.5 h to purge the physically adsorbed species. Finally, the catalyst was heated from 50 to 600 °C at a rate of 10 °C·min^{-1}. The signal of the desorbed gas was detected online with the DX-4000 infrared analyzer. H_2-TPR and O_2-TPD experiments were operated on ChemiMaster 8300. The 50 mg catalyst was pretreated in Ar flow (30 mL·min^{-1}) for 1 h and then cooled to 50 °C. Next, the sample was heated up in 10 % H_2/Ar (30 mL·min^{-1}) from 50 °C to 800 °C at a heating rate of 10 °C·min^{-1} for the H_2-TPR experiment. The 50 mg catalyst was pretreated in 5 vol% O_2/He flow (50 mL·min^{-1}) at 300 °C for 1 h and cooled down to 50 °C, which was followed by purging with He (50 mL·min^{-1}) for 1 h. Then the sample was heated

up from 50 °C to 800 °C at a rate of 10 °C·min^{-1} for the O_2-TPD experiment. *In situ* diffuse-reflectance infrared Fourier-transform spectroscopy (DRIFTS) measurements were conducted on a Bruker Tensor 27 with an MCT detector. The samples were pretreated at 300 °C in N_2 for 1 h before each experiment to remove adsorbed species on the catalyst. The back-grounds were recorded in N_2, and the spectra were acquired at a resolution of 64 scans from 4000 to 1000 cm^{-1} in Kubelka-Munk mode.

2.3. Catalyst activity test

Catalytic activity was evaluated in a fixed-bed quartz reactor (id=6 mm) at atmospheric pressure. 0.40 g (40-60 mesh) catalyst was filled in a quartz tube for each experiment. The reaction gas consisted of 500 ppm C_3H_8, 500 ppm NO, 500 ppm NH_3, 5 vol% O_2, and balanced with N_2. The total flow rate was 200 mL min^{-1}, corresponding to a GHSV of 30,000 mLg^{-1}h^{-1}. The working temperature of the catalyst bed ranged from 150 to 300 °C, and each temperature point was kept for 0.5 h. Stability and SO_2 resistance properties tests were carried out at 250 °C. Reaction conditions were the same as those for activity evaluation. Quantitative analysis of reactants and products was performed online with the DX-4000 infrared analyzer. The NO_x and C_3H_8 conversion were calculated by the following equation:

$$NO_x \text{ conversion } (\%) = \frac{[NO_x]_{in} - [NO_x]_{out}}{[NO_x]_{in}} \quad (1)$$

$$N_2 \text{ selectivity } (\%) = \left(1 - \frac{2[N_2O]_{out} + [NO_2]_{out}}{[NO_x]_{in} + [NH_3]_{in} - [NO_x]_{out} - [NH_3]_{out}}\right) \times 100\% \quad (2)$$

$$C_3H_8 \text{ conversion } (\%) = \frac{[C_3H_8]_{in} - [C_3H_8]_{out}}{[C_3H_8]_{in}} \times 100\% \quad (3)$$

$$CO_2 \text{ selectivity } (\%) = \frac{[CO_2]_{out} - [CO_2]_{in}}{3([C_3H_8]_{in} - [C_3H_8]_{out})} \times 100\% \quad (4)$$

$[NO_x] = [NO] + [NO_2]$

2.5. $^{18}O_2$ isotope experiment

The catalyst was treated in 6 vol% O_2 at 300 °C for 1 h. The gas feed was then

switched to N_2, and the temperature was raised to 450 °C. After being maintained under N_2 at 450 °C for 20 min, the catalyst was exposed to 6 vol% $^{18}O_2$ balanced with N_2 for 30 min to exchange oxygen isotopes with the surface lattice oxygen. The catalyst was then cooled to room temperature under the same $^{18}O_2/N_2$ atmosphere and purged with N_2 to remove residual gas-phase $^{18}O_2$. C_3H_8 oxidation was subsequently conducted in $^{16}O_2$ at 150 and 250 °C. The outlet of the *in situ* infrared reaction cell was connected to an online mass spectrometer, which continuously monitored signals at m/z = 18, 20, 44, 46, and 48 during the reaction.

Supplementary Table 1. The elemental contents of all catalysts in the ICP results

Samples	**A (%)**	**Mn (%)**
$CoMn_2O_4$	25.68	40.45
$NiMn_2O_4$	21.80	41.28
$CuMn_2O_4$	23.50	40.76
$ZnMn_2O_4$	26.41	43.37
$CeMn_2O_x$	38.42	27.22

Supplementary Table 2. BET surface area, pore volume, and average pore size of the catalysts

Samples	**SBET ($m^2 \cdot g^{-1}$)**	**Vpore ($cm^3 \cdot g^{-1}$)**	**Pore Diameter (nm)**
$CoMn_2O_4$	159.37	0.510	13.45
$NiMn_2O_4$	217.55	0.342	6.28
$CuMn_2O_4$	214.08	0.400	7.47
$ZnMn_2O_4$	131.35	0.378	11.52
$CeMn_2O_x$	172.31	0.317	7.35

Supplementary Table 3. The catalytic performance data and apparent activation energy for synergistic removal of NO_x and C_3H_8 over AMn_2O_4 catalysts

Samples	Temperature window		Ea (kJ·mol^{-1})	
	T90 C3H8 (°C)	T > 80% NO_x (°C)	C_3H_8 oxidation	NH_3-SCR
$CoMn_2O_4$	217	150-262	74.74	33.27
$NiMn_2O_4$	219	150-256	71.82	25.51
$CuMn_2O_4$	237	150-229	91.54	33.31
$ZnMn_2O_4$	265	150-270	101.55	37.78
$CeMn_2O_x$	281	150-269	105.82	16.94

Supplementary Table 4. Curie-Weiss fitting parameters derived from the field-cooled (FC) magnetic susceptibility of the AMn_2O_4 catalysts in the temperature range of 200-280 K

Samples	FC (K)	θ (K)	μeff (μB/f.u.)	R2
$NiMn_2O_4$	200-280	-70.3	5.822	0.99803
$CuMn_2O_4$	200-280	0.6	4.943	0.99946
$ZnMn_2O_4$	200-280	-396.2	6.729	0.99969

Supplementary Table 5. Sensitivity analysis of the Curie-Weiss fitting parameters for the AMn_2O_4 catalysts across different temperature windows

Samples	FC (K)	θ (K)	μ_{eff} (μB/f.u.)	R^2
$NiMn_2O_4$	200-280	-70.3	5.822	0.99803
	200-300	-81.5	5.930	0.99735
	220-300	-96.7	6.057	0.99861
	250-300	-116.8	6.217	0.99879
$CuMn_2O_4$	200-280	0.6	4.943	0.99946
	200-300	-3.7	4.988	0.99932
	220-300	-9.3	5.039	0.99956
	250-300	-17.5	5.111	0.99958

$ZnMn_2O_4$	200-280	-396.2	6.729	0.99969
	200-300	-395.6	6.726	0.99979
	220-300	-396.8	6.732	0.99963
	250-300	-391.1	6.703	0.99904

Supplementary Table 6. Mn^{4+}/Mn, O_{ads}/O_{latt} and β- O/O_{total} ratio of AMn_2O_4 catalysts

Samples	Mn^{4+}/Mn	O_{ads}/O_{latt}	β-O/O_{total}
$CoMn_2O_4$	0.729	0.63	0.34
$NiMn_2O_4$	0.771	0.85	0.37
$CuMn_2O_4$	0.723	0.89	0.34
$ZnMn_2O_4$	0.549	0.58	0.26
$CeMn_2O_x$	0.682	0.56	0.45

Supplementary Table 7. The Acidity of AMn_2O_4 catalysts from NH_3-TPD

Samples	Weak acid (μmol g^{-1})	Medium acid (μmol g^{-1})	Strong acid (μmol g^{-1})	Total acid (μmol g^{-1})
$CoMn_2O_4$	86.6	44.5	8.1	139.2
$NiMn_2O_4$	119.4	81.6	11.2	212.2
$CuMn_2O_4$	71.5	57.9	7.6	137.0
$ZnMn_2O_4$	17.5	37.2	10.4	65.1
$CeMn_2O_x$	107.7	54.6	10.8	173.1

Supplementary Table 8. The Area-normalized acid site density of AMn_2O_4 catalysts from NH_3-TPD

Samples	Weak acid (μmol m^{-2})	Medium acid (μmol m^{-2})	Strong acid (μmol m^{-2})	Total acid (μmol m^{-2})
$CoMn_2O_4$	0.5	0.3	0.1	0.9

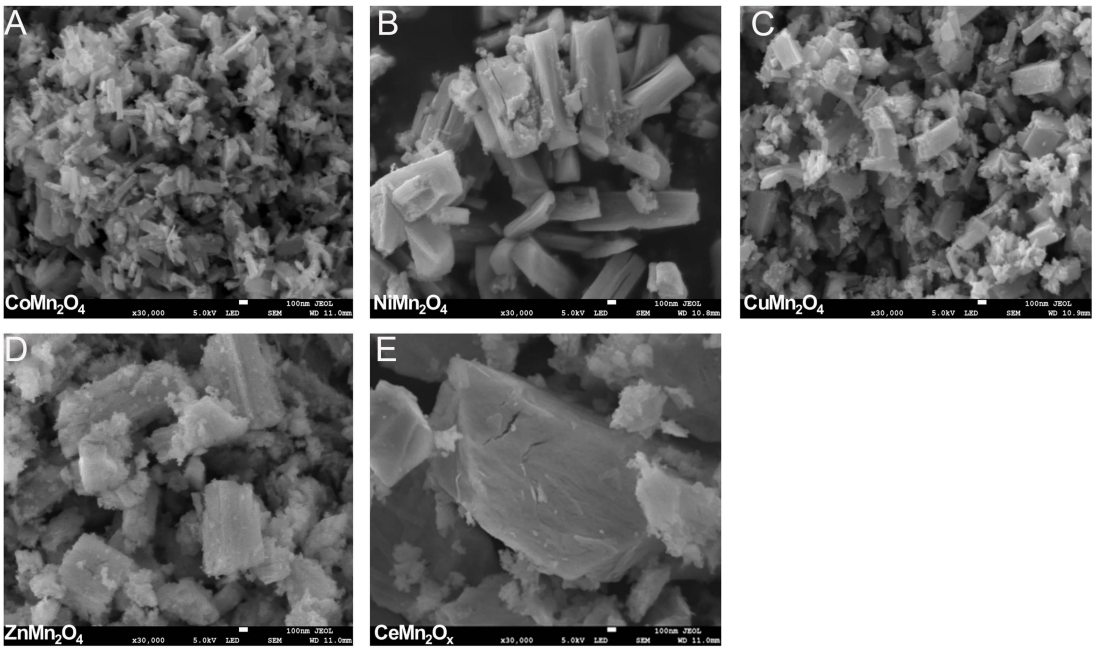
$NiMn_2O_4$	0.6	0.4	0.1	1.1
$CuMn_2O_4$	0.3	0.3	0.0	0.6
$ZnMn_2O_4$	0.1	0.3	0.1	0.5
$CeMn_2O_x$	0.6	0.3	0.1	1.0

Supplementary Table 9. The proportion of L-acid and B-acid determined of NiMn2O4 by pyridine infrared spectroscopy

Samples	L-acid/Total acid	B-acid/Total acid
$NiMn_2O_4$	0.88	0.11

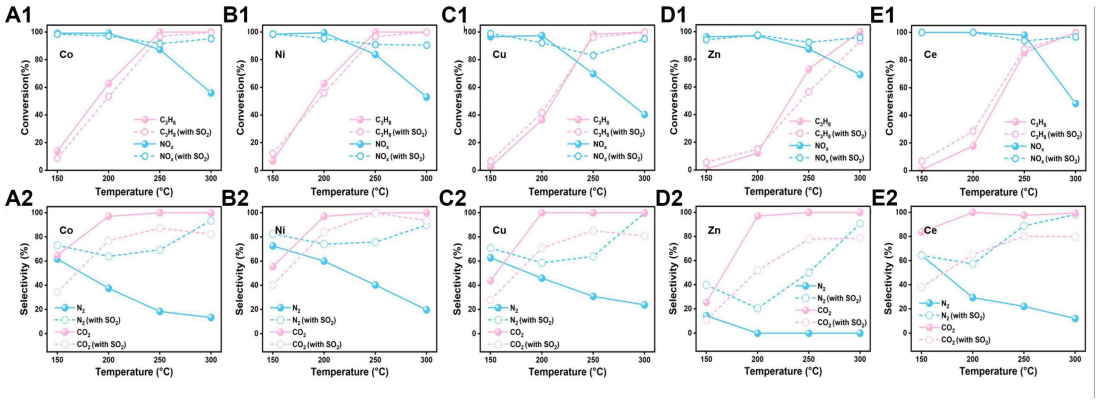
Supplementary Table 10. The Evac, Mn 3d-band and O 2p-band centers of AMn_2O_4 catalysts

Samples	Evac (eV)	Mn d-band(eV)	O p-band (eV)
$NiMn_2O_4$	1.368	-0.785	-2.995
$CuMn_2O_4$	2.858	-1.124	-3.304
$ZnMn_2O_4$	4.714	-1.487	-3.773

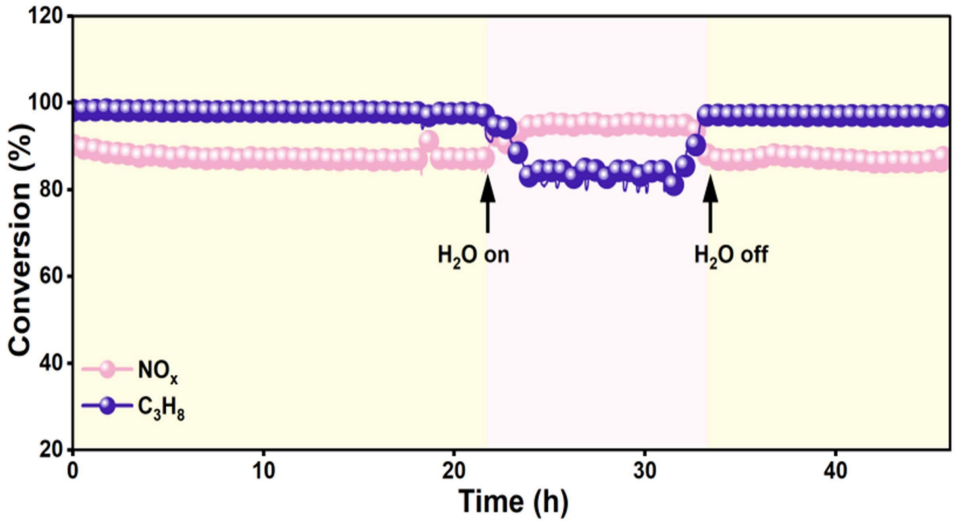


Supplementary Figure 1. (A-E) SEM images of AMn_2O_4 (A = Co, Ni, Cu, Zn, Ce)

catalysts.



Supplementary Figure 2. (A1-E1) C_3H_8 and NO conversions, (A2-E2) CO2 and N2 selectivity of AMn2O4 catalysts. Reaction condition: 500 ppm NH_3, 500 ppm NO, 500 ppm C_3H_8, 40 ppm SO_2 (when used), 5 vol% O_2, N_2 as balance, 30,000 mL g^{-1} h^{-1}. [All figures were generated using Origin (OriginLab Corporation, USA) and Microsoft PowerPoint (Office 365, Microsoft Corporation, USA)].



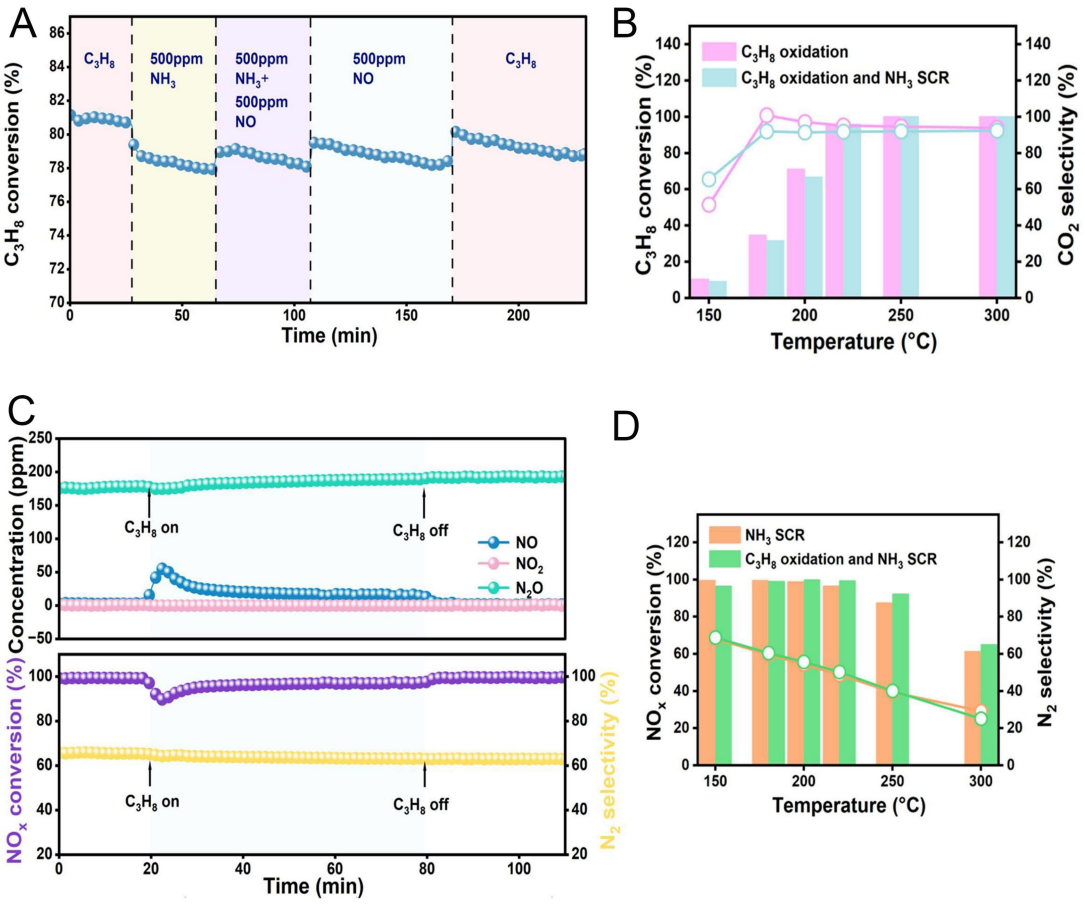
Supplementary Figure 3. Stability testing of $NiMn_2O_4$ catalysts and the effect of water on catalytic activity. Reaction condition: [NH_3] = [NO] = [C_3H_8] = 500 ppm, 5 vol.% O_2, 3 vol.% H2O(when used), N_2 as balance gas, GHSV = 30,000 mL g^{-1} h^{-1}, 250 °C.

The interactions between C_3H_8 oxidation and NH_3-SCR over $NiMn_2O_4$ were

investigated using transient experiments and comparisons between individual and combined reaction feeds [Supplementary Figure 4]. At 250 °C, after propane oxidation had stabilized for 25 min, introducing 500 ppm NH_3 decreased the C_3H_8 conversion from 80.7% to 78.0%. Subsequent addition of 500 ppm NO partially restored the conversion to 78.6%, followed by a further increase to 79.1% upon removal of NH_3. These results indicate a modest inhibitory effect of NH_3 on propane oxidation, consistent with competition for adsorption sites or reactive oxygen species. The partial recovery following NO addition may be associated with the consumption of adsorbed NH_3 through SCR, thereby alleviating this competition. In the separate temperature-dependent activity tests, the combined feed also exhibited slightly lower C_3H_8 conversion than standalone propane oxidation at lower temperatures. At higher temperatures, complete C_3H_8 conversion was achieved under the combined feed, indicating that the SCR components did not prevent complete propane conversion under those conditions.

Conversely, introducing 500 ppm C_3H_8 after 20 min of stable NH_3-SCR operation at 200 °C caused an immediate increase in the outlet NO concentration, with NO_x conversion decreasing from 100% to 89% before gradually recovering to approximately 96%. The NO_2 and N_2O concentrations remained essentially unchanged, and NO_x conversion returned to 100% after C_3H_8 was removed. This reversible response is consistent with competition involving propane or its surface-derived species for adsorption sites or reactive oxygen. Notably, at high temperatures, the NO_x conversion in the co-feed atmosphere did not decrease, demonstrating that propane oxidation has little impact on the SCR reaction at elevated temperatures, allowing both reactions to proceed efficiently without interference. Overall, the individual-feed and combined-feed comparisons reveal modest competitive effects at lower temperatures, while high conversions of both pollutants are maintained within the common operating window. These results demonstrate that $NiMn_2O_4$ can accommodate propane oxidation and NH_3-SCR simultaneously with

limited performance penalties under the tested conditions.

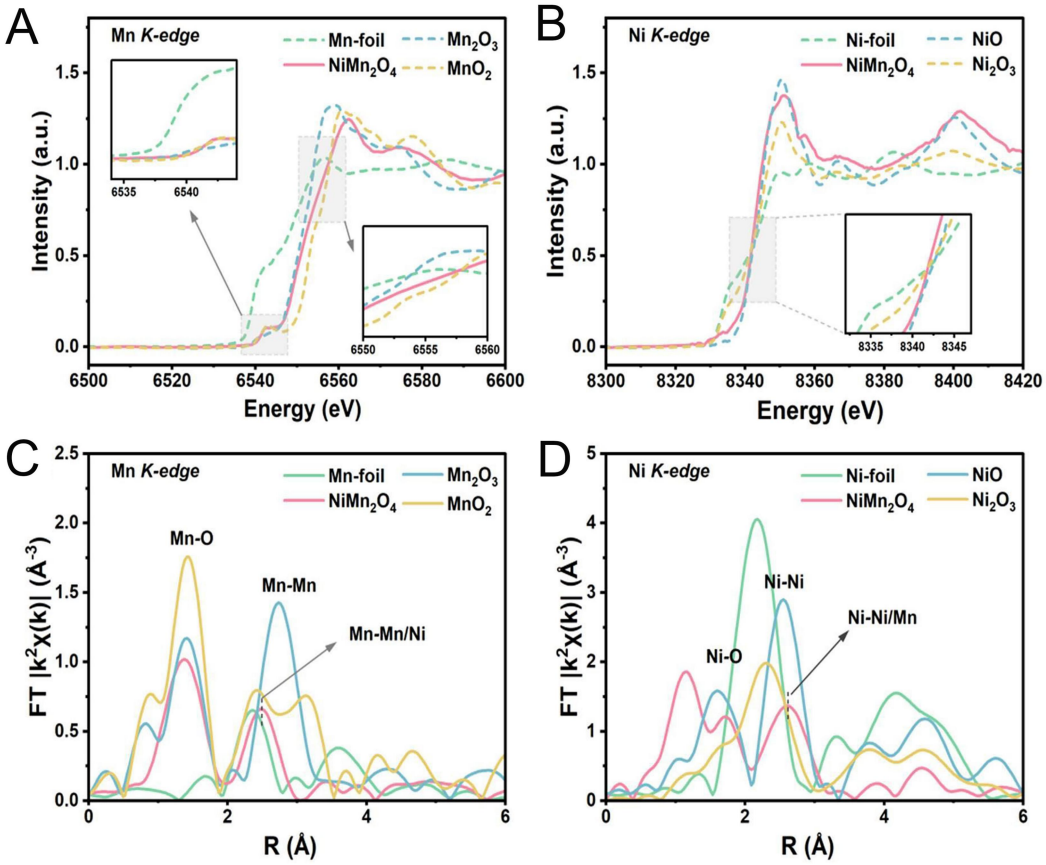


Supplementary Figure 4. (A) Transient experiment over $NiMn_2O_4$ catalyst at 250 °C; (B) C_3H_8 conversions of C_3H_8 oxidation alone and synergistic atmosphere; (C) Effect of propane on the NH_3-SCR reaction over $NiMn_2O_4$ catalyst at 200 °C; (D) NOx conversions of NH_3-SCR alone and synergistic atmosphere. Reaction condition: [NH_3] = [NO] = [C_3H_8] = 500 ppm (when used), 5 vol.% O_2, N_2 as balance gas, GHSV=30,000 mL g^{-1} h^{-1}.

To investigate the distribution of metal cations within the spinel structure, XANES and EXAFS analyses were performed to determine the coordination environments and chemical states of Mn and Ni in the catalyst [Supplementary Figure 5]. The Mn K-edge XANES spectrum of $NiMn_2O_4$ lay between those of Mn_2O_3 and MnO_2 and was overall closer to that of MnO_2, indicating an average Mn oxidation state between

+3 and +4 with a relatively high proportion of Mn^{4+}[1]. In the Ni K-edge XANES spectrum, the absorption edge of $NiMn_2O_4$ was markedly higher than that of Ni foil, indicating that Ni was not present in the metallic state. Its edge position was approximately between those of the NiO and Ni_2O_3 references and was overall closer to that of NiO, suggesting that Ni existed predominantly as Ni^{2+}, with a possible contribution from Ni^{3+}[2]. These results were consistent with the proposed charge redistribution from Ni^{3+}/Mn^{3+} to Ni^{2+}/Mn^{4+}.

Furthermore, Fourier transforms of the k^2-weighted EXAFS spectra were used to analyze the distribution of metal cations. As shown in the figure, the Mn K-edge FT-EXAFS spectrum of $NiMn_2O_4$ exhibited two characteristic peaks at 1.41 Å and 2.48 Å, corresponding to the Mn-O single-scattering path and the Mn-Mn/Ni single-scattering paths involving neighboring metal cations around octahedrally coordinated Mn, respectively. The Ni K-edge FT-EXAFS spectrum exhibited a first-shell Ni-O signal at 1.74 Å and a higher-shell signal at approximately 2.63 Å, which was assigned to Ni-Ni/Mn scattering. These spectral features resembled those of NiO, indicating that Ni predominantly adopted octahedral coordination[2]. Taken together, these results indicated that the system was dominated by a Ni_{oct}-O-Mn_{oct} superexchange network.



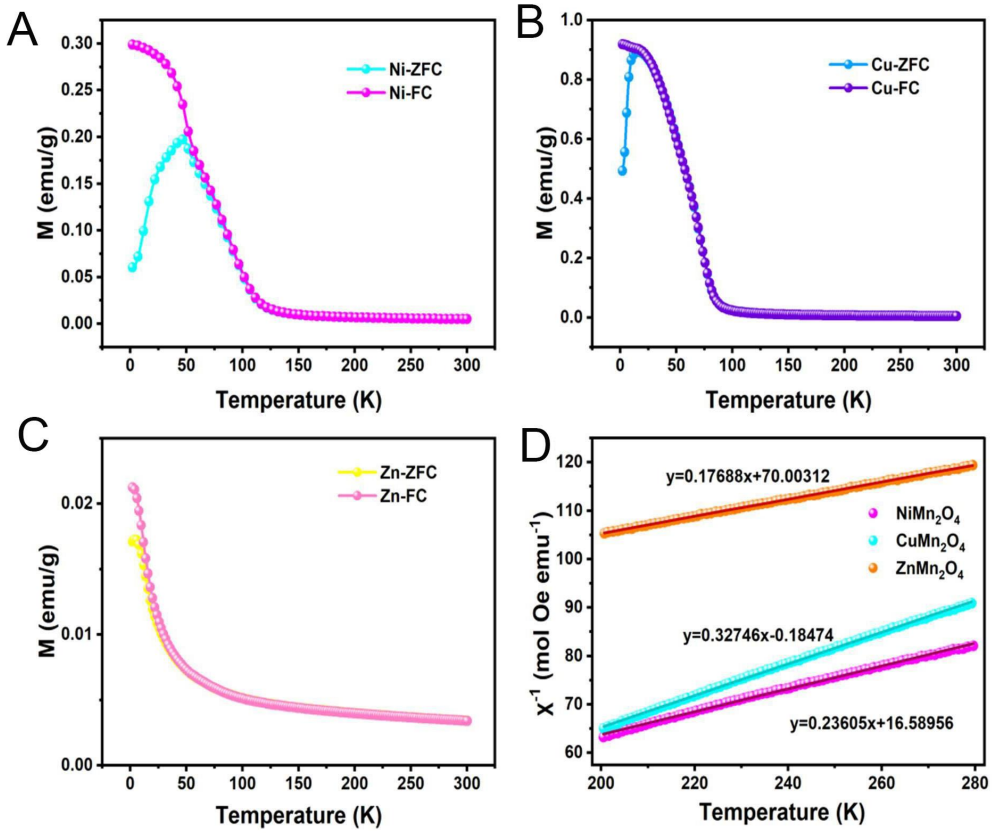
Supplementary Figure 5. XANES spectra at the (A) Mn K-edge (B) Ni K-edge, R-space FT-EXAFS spectra of (C) Mn, (D) Ni of $NiMn_2O_4$.

We have added ZFC/FC magnetic susceptibility measurements for $NiMn_2O_4$, $CuMn_2O_4$, and $ZnMn_2O_4$ at an applied field of 100 Oe over the temperature range of 2-300 K. The high-temperature FC susceptibility data in the range of 200-280 K were fitted using the Curie-Weiss law [Figure 1C and Supplementary Figure 6].

The fitted Weiss temperatures were -70.3 K for $NiMn_2O_4$, +0.6 K for $CuMn_2O_4$, and -396.2 K for $ZnMn_2O_4$, R^2 values of 0.99803, 0.99946, and 0.99969, respectively. The corresponding effective magnetic moments (μ_{eff}) were 5.822, 4.943, and 6.729 μB per formula unit. The negative Weiss temperature of $NiMn_2O_4$ indicates that antiferromagnetic correlations dominate the average magnetic exchange interactions in the high-temperature paramagnetic region. Its pronounced ZFC/FC bifurcation and

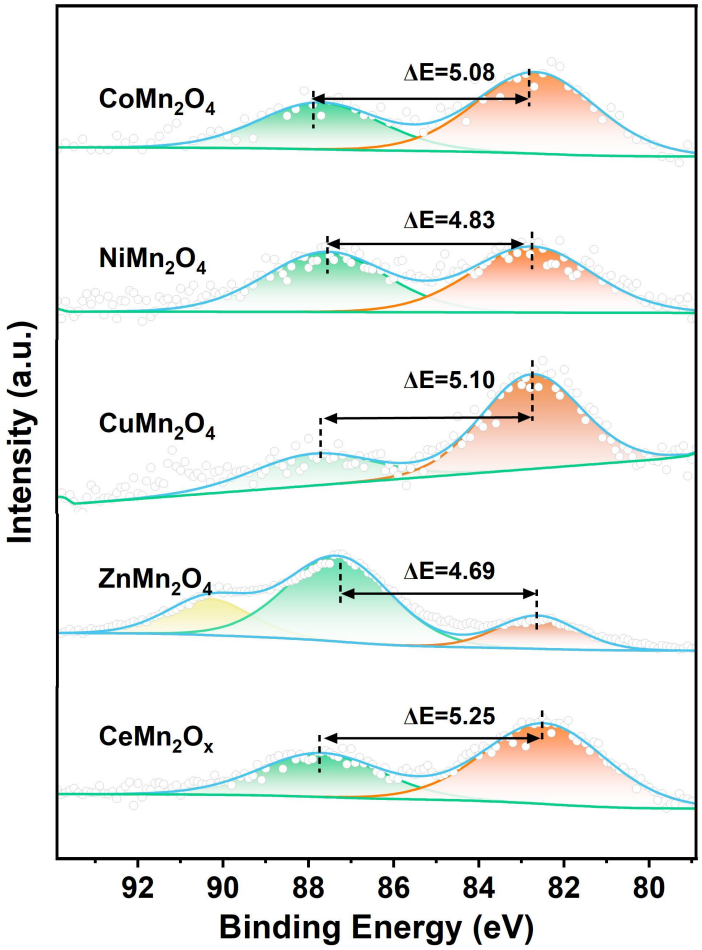
broad ZFC maximum at approximately 45-50 K further indicate low-temperature magnetic irreversibility, which may be associated with canted magnetic ordering, local spin freezing, cation disorder, or magnetic frustration[3].

$CuMn_2O_4$ exhibited a Weiss temperature close to zero, suggesting competition between ferromagnetic and antiferromagnetic interactions. In contrast, $ZnMn_2O_4$ showed a markedly negative Weiss temperature and nearly overlapping ZFC/FC curves. Because Zn^{2+} has a closed-shell d^{10} configuration, its direct contribution to magnetic exchange through Zn-O-Mn is expected to be limited; the strong antiferromagnetic correlations in $ZnMn_2O_4$ are therefore more reasonably associated with exchange interactions within the Mn sublattice, particularly Mn-O-Mn pathways.

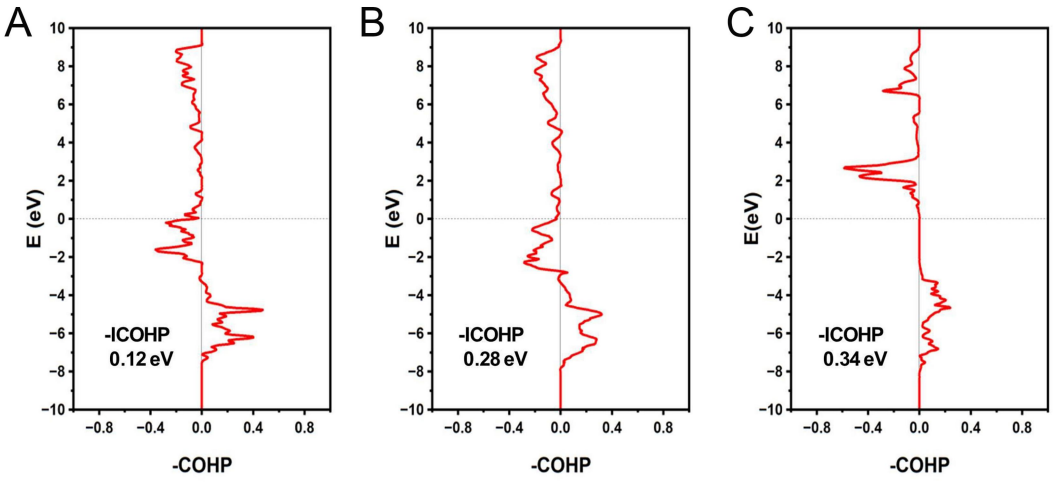


Supplementary Figure 6. (A-C) ZFC and FC magnetization curves of $NiMn_2O_4$, $CuMn_2O_4$, and $ZnMn_2O_4$ (measured at 100 Oe); (D) Curie-Weiss fitting of the inverse

magnetic susceptibility ($1/\chi_m$) for the AMn_2O_4 catalysts in the 200-280 K range.



Supplementary Figure 7. XPS spectra of Mn 3s.



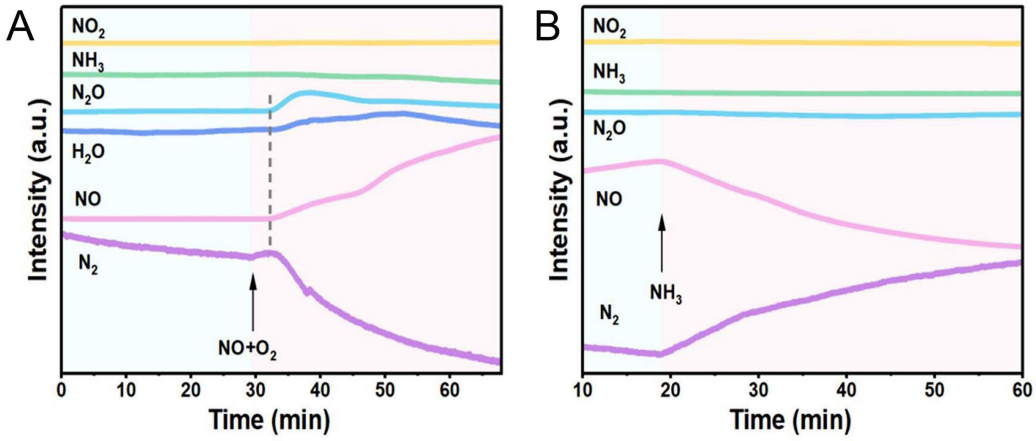
Supplementary Figure 8. Bonding analyses using COHP of Mnoct-O in (A) $NiMn_2O_4$, (B) $CuMn_2O_4$, and (C) $ZnMn_2O_4$.

To further distinguish the Langmuir-Hinshelwood (L-H) and Eley-Rideal (E-R) pathways, and to exclude the possibility of simple desorption or non-reactive site competition, transient DRIFTS coupled with online mass spectrometry (MS) was employed to monitor the gas-phase products. All sequential-feed experiments were conducted isothermally at 230 °C. After the initial adsorption of NO + O_2 (or NH_3) for 30 min, the reactant feed was stopped, and the catalyst was purged with pure N_2 for 10 min. This rigorous purging step eliminates residual gas-phase reactants and physically adsorbed species, ensuring that subsequent reactions occur exclusively between the newly introduced gas and the strongly chemisorbed surface species.
For the L-H pathway verification [Supplementary Figure 9], the catalyst was pre-saturated with NO+O_2. Upon switching the gas flow to NH_3, a continuous attenuation of the NO-related MS signal (m/z = 30) and a sustained, significant increase in the N_2 signal (m/z = 28) were observed. This sustained N_2 evolution, which is further corroborated by the synchronous disappearance of nitrate DRIFTS bands (1218, 1280, 1553, 1564, and 1630 cm^{-1}), indicates that gaseous NH_3 progressively reacts with the pre-adsorbed NO_x species on the surface.

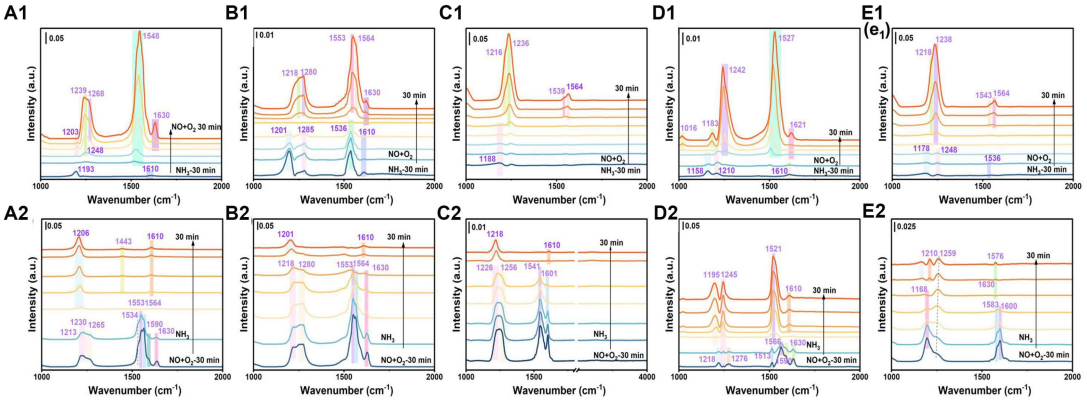
Conversely, for the E-R pathway verification (Figure S9a), when NO + O_2 was introduced to the NH_3 pre-adsorbed surface, the MS exhibited an immediate transient burst of N_2 (m/z = 28), followed by a gradual decay. This initial N_2 burst is the direct signature of gaseous NO reacting rapidly with highly reactive NH_3-derived surface species. The subsequent decay is attributed to the progressive depletion of the pre-adsorbed NH_x species and the gas-switching matrix effect (dilution by the balance gas), which does not obscure the initial N_2 generation pulse.

In conclusion, the monitoring of the transient gas-phase product (N_2) successfully

distinguishes the L-H and E-R pathways, providing definitive evidence for chemical reactions and ruling out simple desorption or non-reactive site competition.



Supplementary Figure 9. Online mass spectrometric analysis of the outlet gas of NO + O_2 reacting with pre-adsorbed NH_3 (A) and NH_3 reacting with pre-adsorbed with NO + O_2 (B) on $NiMn_2O_4$ catalyst at 230 °C.



Supplementary Figure 10. *In situ* DRIFTS of NH_3 reacting with pre-adsorbed NO + O_2 (A1-E1) and NO + O_2 reacting with pre-adsorbed NH_3 (A2-E2) on AMn_2O_4 catalyst (A = Co, Ni, Cu, Zn, Ce).

REFERENCES

[1] L. Chong, G. Gao, J. Wen, La- and Mn-doped cobalt spinel oxygen evolution catalyst for proton exchange membrane electrolysis, Science, 380, (2023) 609-616. https://doi.org/10.1126/science.ade1499

[2] Z. Liu, A. Chen, G. Zhang, et al., Unlocking Activity Origins of High-Entropy Spinel Oxides: Tailoring Octahedral Coordination Chemistry for Accelerated Polysulfide Conversion, Adv Funct Mater, 35, 52 (2025). https://doi.org/10.1002/adfm.202511616

[3] A. Freitas Cabral, J. Peña Serna, B. Salles, H. Amorim, C. Rocha Remédios, M. Novak, Magnetic dynamics of $NiMn_2O_4$ spinel produced by a simple aqueous sol-gel route, J Magn Magn Mater, 538, (2021). https://doi.org/10.1016/j.jmmm.2021.168291